Abnormal Metal Bond Distances in PtAu Alloy Nanoparticles: *In situ* Back-Illumination XAFS Investigations of the Structure of PtAu Nanoparticles on a Flat HOPG Substrate Prepared by Arc Plasma Deposition

Bing Hu,[†] Bapurao Bharate,[†] Juan D. Jimenez,[‡] Jochen Lauterbach, [‡] Naoto Todoroki,[§] Toshimasa Wadayama,[§] Kotaro Higashi,[¶] Tomoya Uruga[¶,¦], Yasuhiro Iwasawa,[¶] Hiroko Ariga-Miwa,[¶] Satoru Takakusagi[†], Kiyotaka Asakura[†*]

[†] Institute for Catalysis, Hokkaido University, Hokkaido 001-0021, Japan

[‡] Department of Chemical Engineering, University of South Carolina, 541 Main St., Columbia, SC 29208, USA

[§] Graduate School of Environmental Studies, Tohoku University, Sendai 980-8579, Japan

[¶] Innovation Research Center for Fuel Cells, University of Electro-Communications, Chofu, Tokyo 182-8585, Japan

[¦]Japan Synchrotron Radiation Research Institute (JASRI), Hyogo 679-5148, Japan

ABSTRACT

To reveal the origin of the difference between the Pt–Pt bond distance in Au(core)–Pt(shell)-type PtAu nanoparticles and that in a Pt overlayer on Au(111), alloy-type PtAu nanoparticles were prepared on a highly oriented pyrolytic graphite (HOPG) surface by arc plasma deposition (APD) and their structure was investigated under various electrochemical conditions by bent-crystal Laue analyzer-empowered back-illuminated X-ray absorption fine structure (BCLA + BI-XAFS) and high-energy-resolution-fluorescence-detection-empowered back-illuminated X-ray absorption near-edge structure (HERFD + BI-XANES) methods. On the basis of the X-ray absorption fine structure (XAFS) analysis at both edges, we proposed the formation of a PtAu alloy core covered with a Pt-rich shell at 0.4 V_{RHE}, where the Pt–Pt, Pt–Au, and Au–Au bond lengths were all found to be ~2.76 Å. The Au–Au bond length was abnormally shorter than that for bulk Au. The Pt shell was dissolved under applied potentials greater than 0.8 V_{RHE} with the aid of the high-intensity X-rays, and the Au–Au distance increased. We concluded that the abnormal bond lengths were due to the strong surface tension from the Pt-rich shell and the relaxation of the lattice distortion. The Pt–Pt bond length in the Au(core)–Pt(shell) nanoparticles decreases as a result of the surface tension of the nanoparticles; this surface tension does not exist on flat Au surfaces, where the lattice distortion between the Pt overlayer and the substrate is the main driving force for the expansion of the Pt–Pt bond length.

INTRODUCTION

Metal nanoparticles exhibit unique electronic properties, such as discrete energy levels and magic number stability originating from quantum mechanics and a high surface/volume ratio.[1] Unique nanoparticle shapes grown from icosahedra, decahedra, and plane triangles have been stabilized to give twin structures.[2,3] Lattice contraction[4-7] and expansion, [8,9] as well as negative thermal expansion,[10] have been reported for nanoparticles. Such characteristics of nanoparticles make them useful in numerous applications, including catalysis, photocatalysis, and magnetic and electronic devices.[11]

Pt nanoparticles are used in the cathode of hydrogen fuel cells for the oxygen reduction reaction (ORR). Hydrogen fuel cells can potentially meet the soaring demand for a green energy source with a high output efficiency and zero emissions, and the bottleneck of the technology is the scarcity of Pt, which makes the commercialization of fuel cells expensive.[12] Enhancing the activity and stability of Pt nanoparticles to reduce the amount of Pt has been an active topic in fuel cell research.[13] One promising method is to prepare PtAu bimetallic nanoparticles. Capping Pt nanoparticles with Au atoms has been reported to greatly enhance the durability of Pt in the acidic conditions of the ORR.[14,15] Au(core)–Pt(shell) structures have been prepared to achieve greater Pt utilization.[16,17,18,19,20-21] In addition to enhancing the Pt mass activity, the activity per surface Pt atom was improved in Au(core)–Pt(shell) structures. An enhancement of the activity per surface Pt atom was observed in other metal(core)–Pt(Shell) systems, where the greater activity was attributed to a shorter Pt–Pt interatomic distance.[22,23,23] However, the enhancement of activity per surface Pt atom on Au in a core–shell structure was unexpected because Pt was predicted to have a longer bond length in the shell region, thus resulting in lower activity.[24] The Pt–Pt distance in bulk Pt is 2.76 Å, whereas the Au–Au distance in bulk Au is 2.86 Å; thus, a Pt monolayer deposited onto a Au surface should have a longer bond length. Actually, according to the literature, the Pt–Pt distance in a Pt monolayer on Au(111) is longer than that in bulk Pt and the monolayer structure is less active.[25,26-27]

X-ray absorption fine structure (XAFS) is a powerful technique for determining metal–metal bond distances in nanoparticles.[28] However, using XAFS to characterize Au(core)–Pt(shell) nanoparticle systems is difficult because of the interference between the Pt and Au L_3 edges.[29] Kaito et al.[21] reported K-edge Pt and Au XAFS spectra of PtAu nanoparticles whose edges were separated by 2400 eV; the interference was therefore negligible. They observed a Au(core)/Pt(shell) structure in the PtAu nanoparticles. They also found that the Pt–Pt and Au–Au distances were contracted by 0.03 Å and 0.04 Å, respectively, from those of Pt and Au bulk metals. They concluded that, compared with Pt/C, the Au(core)–Pt(shell) nanoparticle structure exhibited greater activity per surface Pt atom for the ORR.

Here, we address a simple question: Why does the Pt–Pt distance in the Au(core)–Pt(shell) nanoparticles contract, whereas the Pt–Pt distance in a Pt monolayer on a Au(111) surface does not? Bond-length contraction has been reported for various metal nanoparticles.[4-6] Although Kaito et al.[21] found that the Au–Au bond length in the Au core of Au(core)–Pt(shell) nanoparticles was contracted by 0.04 Å to a value of 2.82 Å, this is still longer than the Pt–Pt bond length in bulk Pt (2.76 Å). If the surface-layer bond length (Pt–Pt) strongly depends on the bond length in the substrate (Au–Au), as it does in the case of a flat surface, then the Pt–Pt distance should be elongated because of the effect of the Au core. Thus, the Pt–Pt bond distance is not solely determined by the substrate structure. To confirm the influence of the substrate's geometrical and electronic effects, we prepared well-mixed PtAu alloy nanoparticles. The PtAu alloy nanoparticles should have a smaller lattice spacing, which might result in a Pt–Pt bond length that is shorter than that for Pt on a pure Au core structure.

In the bulk PtAu binary system, phase separation has been reported to occur through the formation of unstable intermetallic states.[30-32] However, PtAu metal alloy nanoparticles have been found to form in both theoretical and experimental studies.[33-36] Whether surface segregation or alloy formation occurs depends on the synthesis conditions.[37] In the present study, we used the arc plasma deposition (APD) method to prepare PtAu alloy nanoparticles. APD can generate pure metal or binary nanoparticles by blowing ionized metal plasma, where the morphology and composition of the nanoparticles are controlled by changing the blowing sequence, number of pulse repetitions, and the applied voltage.[15] To obtain PtAu alloy nanoparticles, two arc plasma guns with Au and Pt sources are used to deposit Au and Pt simultaneously. To obtain deposited nanoparticles with a homogenous size and composition, the APD process requires a flat surface, such as that of highly oriented pyrolytic graphite (HOPG). Unlike the powdery carbon supports used in numerous previous XAFS studies,[16,38-44] PtAu nanoparticles deposited onto the flat HOPG could not be easily characterized by XAFS because of their low loading of Pt and Au (~10^{15} cm^{-2}). For the surface state to be controlled, the sample must be kept under an inert gas, under ultrahigh vacuum, or immersed in an electrolyte under a controlled electrochemical potential. Given the potential applications of PtAu nanoparticles in fuel cells, we selected the controlled-potential electrolyte environment in the present study. However, the coexisting electrolyte strongly absorbs X-rays and creates undesirable scattered X-rays that adversely affect the quality of the acquired XAFS spectra.

We recently developed the bent-crystal Laue analyzer (BCLA)-empowered back-illuminated XAFS (BCLA + BI-XAFS) technique that enables XAFS measurements of ~10^{15} cm^{-2} Pt on a flat HOPG surface.[45] We can fabricate thin HOPG substrates suitable for use as a substrate for nanoparticles, as a window for X-rays, or as an electrode for electrochemistry. The Pt nanoparticles are irradiated by X-rays from the HOPG window

side so that absorption by the electrolyte can be neglected. The BCLA can select only Pt L_α fluorescent X-rays, and remove X-rays due to scattering and fluorescence from other elements. Consequently, we can acquire spectra with a higher signal-to-background (S/B) ratio.

The BCLA + BI-XAFS technique offers four main advantages in the analysis of PtAu nanoparticles:

(1) The electrolyte thickness has no limitation because fluorescence X-rays are detected from the backside of the substrate window, minimizing the effects of absorption and elastic scattering by the electrolyte.
(2) *In situ* measurements can be carried out under electrochemical conditions to characterize the structure of PtAu nanoparticles under controlled electrochemical conditions.
(3) The HOPG surface is atomically flat, which enables characterization via surface science techniques such as X-ray photoelectron spectroscopy (XPS), atomic force microscopy (AFM), and scanning tunneling microscopy (STM).
(4) The interference of the L_3 edges of Pt and Au can be eliminated by separating the Au and Pt fluorescence X-rays.[46]

In the high-energy-resolution-fluorescence-detection (HERFD)-empowered back-illuminated X-ray absorption near-edge structure (HERFD + BI-XANES) method, another type of crystal monochromator is adopted to reduce the lifetime broadening effect and obtain high-energy-resolution XANES spectra that provide more precise information about the electronic state. HERFD + BI-XANES spectra can be obtained by replacing the BCLA with a Johan-type crystal analyzer.

In the present work, we carried out *in situ* BCLA + BI-XAFS and *in situ* HERFD + BI-XAFS measurements on PtAu alloy nanoparticles prepared by APD to elucidate the effect of alloying on the bond length. By manipulating the electrochemical potential, we obtained an electrochemically clean surface. We found that the thus-obtained PtAu cluster had a unique PtAu (core)–Pt(shell) structure in which the Pt–Pt , Au–Au, and Pt–Au distances are all ~2.76 Å, which is approximately the same as the Pt–Pt distance in Pt foil and is abnormally 0.1 Å shorter than the Au–Au bond length in Au foil. We discuss the abnormally short Au–*M* (*M* = Au, Pt) bond length from geometric and electronic perspectives, along with the difference in the overlayer Pt–Pt bond length between a flat surface and a nanoparticle.

EXPERIMENTAL METHODS

Preparation of the PtAu/HOPG Model Catalyst

The surface of a 2 × 2 cm^2 HOPG sample with a thickness of a few micrometers was peeled several times using Scotch tape to obtain an atomically flat surface. The sample was transferred into an ultra-high vacuum (UHV) (~10^{-8} Pa) chamber and annealed at 773 K to clean the HOPG surface. Pt and Au were then simultaneously deposited onto the HOPG surface using Pt and Au APD guns (ULVAC-RIKO ARL-300) with applied voltages of 100 and 70 V, respectively. The PtAu-deposited sample was then transferred from the UHV-APD chamber into an Ar-filled glovebox, where it was finally sealed in an Ar-filled sample box (Figure S1) to avoid exposure to air. The sample is hereafter denoted as PtAu/HOPG. Pt-deposited carbon (Pt/HOPG) was prepared in the same manner (APD) for reference.

AFM, XPS, and CV Measurements

The surface morphology of the PtAu nanoparticles on the HOPG was imaged by AFM (Cypher, Oxford Instruments). The Pt and Au loadings on the PtAu/HOPG were determined by XPS analysis using a JEOL JPC-9010MC X-ray photoelectron spectrometer equipped with a Mg Kα (1253.6 eV) X-ray source operating at 10 kV and 10 mA.

To obtain information about the exposed Pt surface area, cyclic voltammetry (CV) experiments were conducted in 0.1 M $HClO_4$ inside a glass electrochemical cell connected to a potentiostat (HSV-110, Hokuto Denko, Tokyo, Japan). The backside of the PtAu/HOPG sample was connected to a Pt hook, and the PtAu-coated front face contacted the electrolyte in a meniscus fashion. The counter electrode was a Pt coil, and a reversible hydrogen electrode (RHE) was used as the reference electrode. CV was conducted between 0.05 and 1.45 V vs. RHE (referred to as V_{RHE} hereinafter). The exposed Pt surface area was evaluated on the basis of the hydrogen underpotential deposition (HUPD) zone.

In situ BCLA BI-XAFS Measurements

After our preliminary studies in PF(Photon Factory in KEK), *in situ* XAFS measurements were carried out at the BL36XU beamline at SPring-8 (Super Photon ring-8 GeV, JASRI, Japan), one of the most brilliant beam line in SPring-8. To avoid air

oxidation, the PtAu/HOPG sample was mounted on a homemade electrochemical and XAFS-measurement cell inside a N_2-filled glovebox. Figure 1 shows a schematic of the cell and the BCLA + BI-XAFS setup. Details are given in Figures S2 and S3 as well as in Supplementary Text 1. The PtAu/HOPG was used as an X-ray window, and the HOPG front side with PtAu was directed inward toward the cell, contacting the electrolyte. Each Pt L_α or Au L_α fluorescent X-ray signal was distinguished by the BCLA from other signals and from undesired scattered X-rays. Fluorescence lines were selected by adjusting the position of the BCLA. The monochromatized fluorescence signals were collected by a 25-element Ge solid-state detector (SSD).

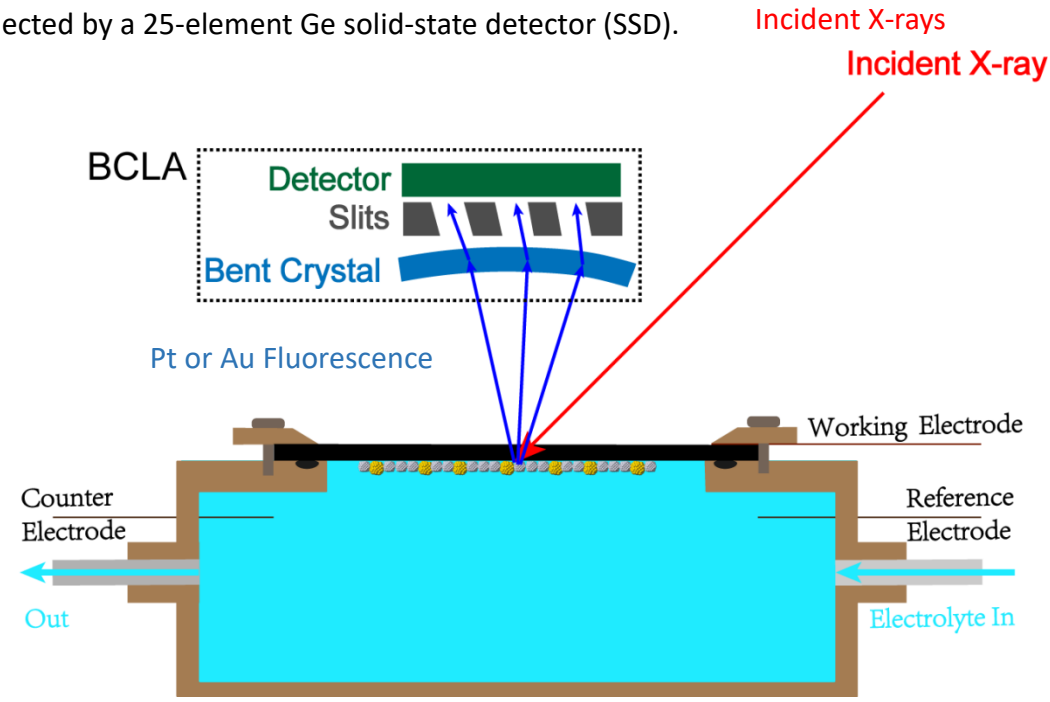

Figure 1 Schematic of the BCLA + BI-XAFS setup for the *in situ* XAFS measurements in the present work. Changing the BCLA position enabled selection of Pt or Au fluorescence.

We used an RHE as the reference electrode and 0.1 M $HClO_4$ as the electrolyte. The incident X-ray angle was set to 45° with respect to the HOPG surface (near the magic angle) to reduce the polarization dependence. Before the XAFS measurements, the desired potential was applied to the working electrode to reach electrochemical equilibrium. The Pt L_3-edge and Au L_3-edge XAFS measurements were then started, with the same potential being maintained throughout the measurements. At each potential, the Pt L_3 or Au L_3 XAFS data were accumulated with several scans and the averaged XAFS analysis was performed using the REX 2000 program (Rigaku).[47] The details are provided in Supplementary Text 1.

In situ HERFD + BI-XANES Measurements

The HERFD + BI-XANES measurements were carried out using the same BI-XAFS cell, except that the BCLA was replaced by eight sets of Johan type Ge(660) bent crystals so that the Pt L_α fluorescence (9442 eV) was selected with high resolution. The fluorescence X-rays were detected by a two-dimensional pixel array detector (Merlin Quad, Quantum Detector). With this configuration, an energy resolution of 1.2 eV was attained.[48]

RESULTS AND DISCUSSION

Microscopic Morphology of the PtAu/HOPG Surface

Figure 2a shows an AFM image of the PtAu/HOPG. Because the observed lateral size of the particles was larger than their actual lateral size as a consequence of the tip-effect, we estimated the particle size from more reliable height information under the assumption that the particles were spherical. Figure 2b shows the height distribution of the PtAu particles on the HOPG substrate. The diameter of the PtAu nanoparticles was ~1.8 nm on average.

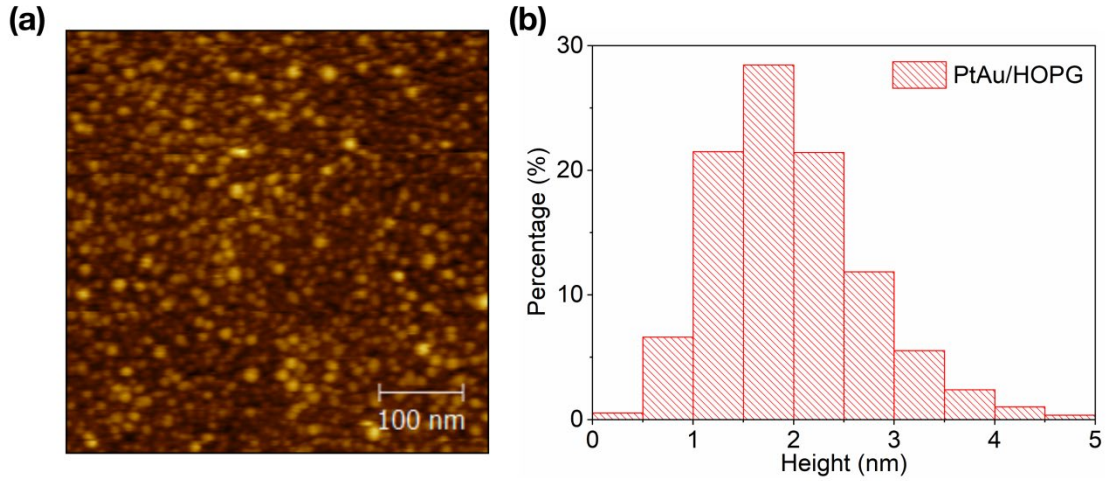

Figure 2 (a) AFM image (0.5 µm × 0.5 µm) of the PtAu/HOPG model surface. (b) Distribution of the height of the PtAu particles on the HOPG surface.

Quantification of Pt on the PtAu/HOPG

Figure S4 shows the XPS spectra, which indicate a Pt loading of 2.0×10^{15} cm^{-2} and

an Au loading of 0.8×10^{15} cm^{-2} on the surface of the HOPG (Supplementary Text 2). The Pt:Au atomic ratio was 2.5.

After the XPS analysis, we recorded cyclic voltammograms of the PtAu/HOPG sample in 0.1 M $HClO_4$ at a scan rate of 50 mV s^{-1}. The characteristic features of HUPD at potentials less than ~0.4 V_{RHE} and the cathodic peak at 0.7 V corresponding to the reduction of Pt–O in polycrystalline Pt are observed in the cyclic voltammogram in Figure 3. In addition, the cathodic current peak at 1.2 V is ascribed to the reduction of surface Au–O because the upper potential limit during CV was 1.45 V, which is sufficient to oxidize the (100) and (110) facets of Au.[49,50]Integration of the Pt–O reduction peak gave a charge density of 192 µC cm^{-2}, whereas integration of the reduction peak for Au–O gave a charge density of 9.25 µC cm^{-2} (Figure S5), indicating that Pt was more abundant than Au on the surface of the PtAu/HOPG. The HUPD charge density of 112 µC cm^{-2} obtained by integrating the potential window from 0.37 V to 0.06 V with a baseline of double-layer current indicates that the areal density of Pt atoms on the surface of the PtAu nanoparticles was 7.9×10^{14} cm^{-2}. Because the size of PtAu nanoparticles obtained by AFM was 1.8 nm, we estimated that the ratio between the number of surface atoms and the number of atoms in a whole particle was ~50%.[51] Thus, the total amount of Pt on the HOPG should be ~1.6×10^{15} cm^{-2}, which is similar to the XPS-derived areal density of Pt.

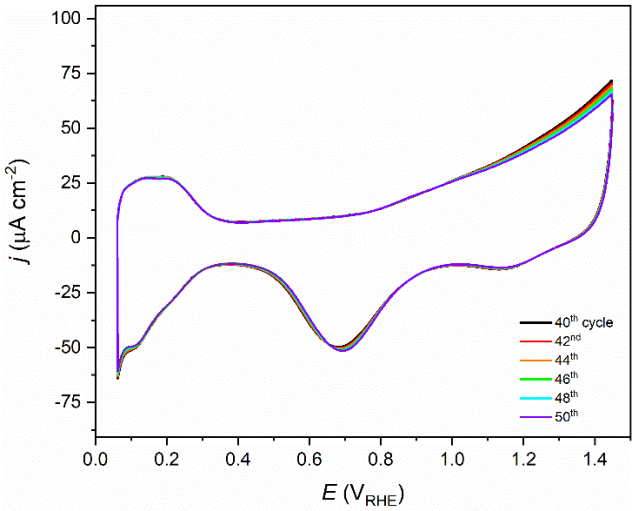

Figure 3 Cyclic voltammograms for PtAu/HOPG in 0.1 M $HClO_4$, as recorded at a scan rate of 50 mV s^{-1} between 0.06 and 1.45 V_{RHE}.

BCLA + BI-XAFS of Both Pt and Au L_3-edge XAFS

The L_3 edge is superior to the K edge because of the availability of stronger X-ray sources emitted from the undulator and the high energy resolution; however, the Pt and

Au L_3 edges overlap because of their close proximity. In our previous work,[46,5252] we demonstrated that BCLA can completely separate the Au L_α and Pt L_α fluorescence X-rays, enabling an analysis of the Pt XAFS in the *k*-range beyond 10 $Å^{-1}$. The Pt:Au atomic ratio in the PtAu/HOPG was 2.2, as determined from the edge step analysis (Table S1), and was consistent with the results of the XPS analysis. Note that the Au effect was negligible when the amount of Au was very small so that its absorption and the inelastic scattering of Au fluorescence X-ray were negligible. Otherwise, the range-extended XAFS would be impossible [52]even if one uses the fluorescence spectrometer.

Figure 4 shows the k^2-weighted $\chi(k)$ of PtAu/HOPG at 0.4 V_{RHE}, together with those for Pt foil and Au foil. The Pt L_3 XAFS oscillation for PtAu/HOPG at 0.4 V_{RHE} exhibited almost the same periodicity as that for Pt foil in the range from 3 to 14 $Å^{-1}$, indicating a Pt–*M* bond length similar to that observed for Pt foil. However, the Au L_3-edge XAFS oscillation had a longer wavelength than that for the Au foil, and was similar to that for the Pt foil, indicating a shorter Au–*M* bond in the PtAu nanoparticles than in the Au foil. Consequently, the Pt–*M* and Au–*M* distances in the PtAu nanoparticles should both be ~2.76 Å, similar to the Pt–Pt distance in Pt foil. The XAFS amplitude of the Au L_3 edge was approximately the same as that for the Au foil, whereas the amplitude of the Pt L_3 edge was smaller than that for the Pt foil, indicating the Pt in the PtAu/HOPG likely has a coordination number (CN) less than 12, whereas that of Au is likely close to 12.

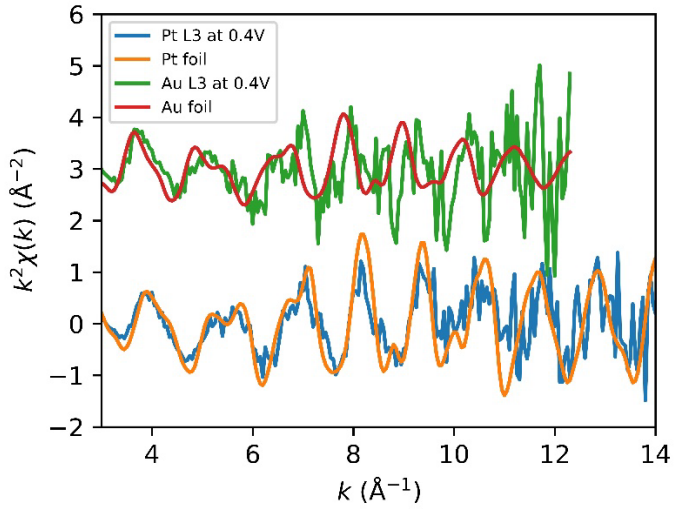

Figure 4 Pt L_3 and Au L_3 k^2-weighted XAFS oscillation ($k^2\chi(k)$) for PtAu/HOPG at 0.4 V_{RHE} in comparison with the oscillations for the foil references.

Further analyses were carried out by nonlinear least-squares fitting. Because the Pt and Au exhibited approximately the same backscattering amplitude and phase-shift functions, the Pt and Au shells are difficult to analyze separately. We analyzed a single shell to characterize the average structures around Pt and Au. The results are presented in Table 1 (see also Figure S6). The uncertainties of the fitting parameters listed in the

table were derived from χ^2- test,[53, 54] described in Supplementary Text 3 and Figure S10. The Pt–*M* bond length was 2.75 ± 0.02 Å, which is similar to that for bulk Pt, whereas the CN was 8.6 ± 1.6, which is lower than the CN for 12 for bulk Pt. The Au–*M* bond length was 2.76 ± 0.03 Å, and the CN for Au was 11.0 ± 2.2 (i.e., nearly 12).

When the electrode potential was increased from 0.4 V_{RHE} to 0.7 V_{RHE}, the Pt–*M* and Au–*M* distances did not substantially change. The CN and bond length for Pt increased at 0.8 V_{RHE} and 0.9 V_{RHE} (Table 1). However, from the Au L_3 edge spectrum, the CN for Au suddenly decreased at 0.9 V_{RHE} and the Au–*M* length increased to 2.80 Å.

The structural change that occurred at potentials greater than 0.8 V_{RHE} can be explained by two possibilities: (1) a change in the adsorbate or the oxidation state or (2) the selective dissolution of Pt. The Pt edge height decreased dramatically when an electrochemical potential more positive than 0.8 V_{RHE} was applied, indicating remarkable dissolution of Pt. The Pt L_3 edge height at 0.9 V_{RHE} was 48% of that at 0.4 V_{RHE} (Table S1), whereas the Au L_3 edge height at 0.9 V_{RHE} was 92% of that at 0.4 V_{RHE}. After increasing the potential to 1.0 V_{RHE}, we returned the electrode potential to 0.4 V_{RHE} and found that the irradiated position was shifted by a few millimeters and the edge height ratio for Au L_3 and Pt L_3 recovered to its original value of 2.3. On the basis of the size of the beam at BL36XU (approximately 0.5 mm × 0.03 mm), the dissolution of Pt was enhanced by irradiation by X-rays, and the irradiated part was mainly dissolved. Figure S7 shows the spectra for the first and the last scan at 0.4 V_{RHE} and 0.8 V_{RHE}, respectively. At 0.4 V_{RHE}, little dissolution was observed, whereas at 0.8 V_{RHE}, the edge height decreased after the measurement. The dissolution of Pt required both X-ray irradiation and a potential greater than 0.8 V_{RHE}.

Pt/HOPG prepared in the same manner exhibited a Pt–Pt distance of 2.73 ± 0.02 Å with a Pt CN of 7.1 ± 1.8. We observed the dissolution phenomenon using a similar approach. As expected, the Pt–Pt bond contracted. The smaller CN indicates a smaller particle size of ~1 nm.

Table 1 Curve-fitting results for the Pt and Au XAFS spectra

	L_3 Edge	Shell	CN	*d* (Å)	dE_o (eV)	σ^2 (Å^2)	S_o^2	*R*-fac (%)
PtAu/HOPG 0.4 V_{RHE}	Pt	Pt–*M*	8.6±1.6	2.75±0.02	5.1*	0.0070±0.0010	1.12*	0.2
	Au	Au–*M*	11.0±2.2	2.76±0.03	0.5*	0.0111±0.0027	0.94*	0.4
PtAu/HOPG 0.5 V_{RHE}	Pt	Pt–*M*	8.6±1.7	2.76±0.02	5.1*	0.0068±0.0011	1.12*	1.3
	Au	Au–*M*	11.0±2.6	2.77±0.04	0.5*	0.0099±0.0032	0.94*	4.3
PtAu/HOPG 0.7 V_{RHE}	Pt	Pt–*M*	8.9±1.8	2.76±0.02	5.1*	0.0073±0.0011	1.12*	0.2
	Au	Au–*M*	9.9±2.4	2.78±0.04	0.5*	0.0092±0.0031	0.94*	3.2
PtAu/HOPG 0.8 V_{RHE}	Pt	Pt–*M*	9.7±1.9	2.77±0.02	5.1*	0.0071±0.0012	1.12*	0.7
	Au	Au–*M*	9.6±3.3	2.79±0.03	0.5*	0.0081±0.0030	0.94*	3.5
PtAu/HOP	Pt	Pt–*M*	10.4±3.0	2.77±0.03	5.1*	0.0090±0.	1.12*	1.5

G 0.9 V_{RHE}	Au	Au–*M*	7.3±3.5	2.80±0.04	0.5*	0027 0.0073±0. 0028	0.94*	3.5
Pt/HOPG 0.4 V_{RHE}	Pt	Pt–*M*	7.1±1.8	2.73±0.02	5.1*	0.0067±0. 0014	1.12*	2.6
Pt Foil	Pt	Pt–Pt	12*	2.76±0.01	5.1±2.0	0.0057±0. 0011	1.12±0.18	0.6
Au Foil	Au	Au–Au	12*	2.86±0.01	0.5±1.7	0.0083±0. 0011	0.94±0.13	0.6

* Parameters that were fixed during fitting. CN: coordination number; *d*: bond length; dE_o: absorption edge shift; σ^2: Debye–Waller factor; S_o^2: the effective reduction factor as shown in eqn S2 in SI. We used the FEFF-calculated inelastic scattering factor λ in eqn (S2) so that the S02 exceeds 1 in Pt foil case. .

The k-range for FT is 3.0 – 14.0 Å-1 for Pt L3 (c) and 2.5 – 8.5 Å-1 for Au L3 (e). The R-range for back-k fitting is 1.8 – 3.1 Å for Pt L3 (b) and 1.6 – 3.4 Å for Au L3 (d). *M*(number of information)=11 for Pt and =9 for Au edge.

XANES Analysis of PtAu/HOPG

To examine the effect of the electronic properties of the PtAu/HOPG on the change of the bond lengths under the different applied potentials, we compared the XANES spectra recorded at different potentials. Figure 5a shows the XANES spectra of PtAu/HOPG under different potentials and the spectrum of Pt foil, as acquired using the BCLA + BI-XAFS method. Little difference is observed between the spectrum of PtAu/HOPG at 0.4 V_{RHE} and that of Pt foil. The change was smaller than that for Pt/HOPG (Figure S8). When the potential was increased to 1.0 V_{RHE}, the white-line intensity in the *in situ* BCLA + BI-XAFS spectra increased slightly (Figure S8). The Au L_3-edge XANES spectra corresponding to 0.4 and 1.0 V_{RHE} showed no obvious difference. Thus, the change in the electronic state was not large in the change of potential, and the change in the Au–*M* bond length was not due to the change in electronic state nor the effect of the adsorbate.

To obtain additional details, we carried out Pt L_3-edge HERFD + BI-XAFS measurements.[55] In the BCLA, the energy resolution was 10 eV greater than the natural width of the L_3 ($2p_{3/2}$) level (5.31 eV),[56] whereas the Ge crystal monochromator (1 eV energy resolution) reduced the lifetime broadening. Because of the monochromator limitation, we could not record Au L_3-edge HERFD + BI-XAFS spectra; we therefore only discuss the change of the Pt L_3-edge XANES spectra. Figure 5b shows the HERFD + BI-XAFS of Pt/HOPG and PtAu/HOPG prepared by APD. In the PtAu bimetallic system, the Pt edge peak slightly decreases, indication of the modification of Pt electronic state. Figure 5c shows the potential dependence of Pt HERFD+BI-XAFS. We could not observe a clear difference with potentials, indicating that the Pt electronic state did not substantially change, similar to what we observed in the *in situ* BCLA + BI-XAFS experiment. However, we observed changes in the difference spectra (Figure 5d). The

changes are consistent with the effects of adsorbates reported in the literature.[57,58] The spectrum corresponding to an applied potential of 0.4 V_{RHE} corresponds to the double-layer region, where the surface of Pt can be regarded as nearly metallic. Pt–H was formed at 0.1 V_{RHE}, Pt–OH began to form at 0.6 V_{RHE} and increased in abundance at 0.8 V_{RHE}, and then Pt–O formed at 1.0 V_{RHE}. We found that, at 0.1 V_{RHE}, the white-line peak region between 11,565 and 11,569 eV decreased in intensity compared with that at 0.4 V_{RHE}. This feature is consistent with the Pt L_3 XANES spectra reported for H-chemisorbed Pt nanoparticles[59-62] but with less extensive chemisorption. At 0.6 V_{RHE}, a slight increase in the white-line region was observed between 11,565 eV and 11,570 eV; at 0.8 V_{RHE}, this peak was further enhanced. Thus, the change corresponded to the adsorption of OH. At 1.0 V_{RHE}, the peak height increased and shifted to 11,570 eV with broadening, which might be due to the adsorbed O. To better interpret such subtle changes in the HERFD + BI-XANES spectra, we compared the changes of the HERFD-XANES spectra with those calculated by the FEFF8 program. Preliminary results were given in Supplementary Text 4 and Figure S11-12. Although the calculation work is still undergoing, we tentatively concluded that OH adsorption at 0.8 V_{RHE} was on the bridge site and O adsorption at 1.0 V_{RHE} was on the bridge site or the atop site. Further studies must be necessary.

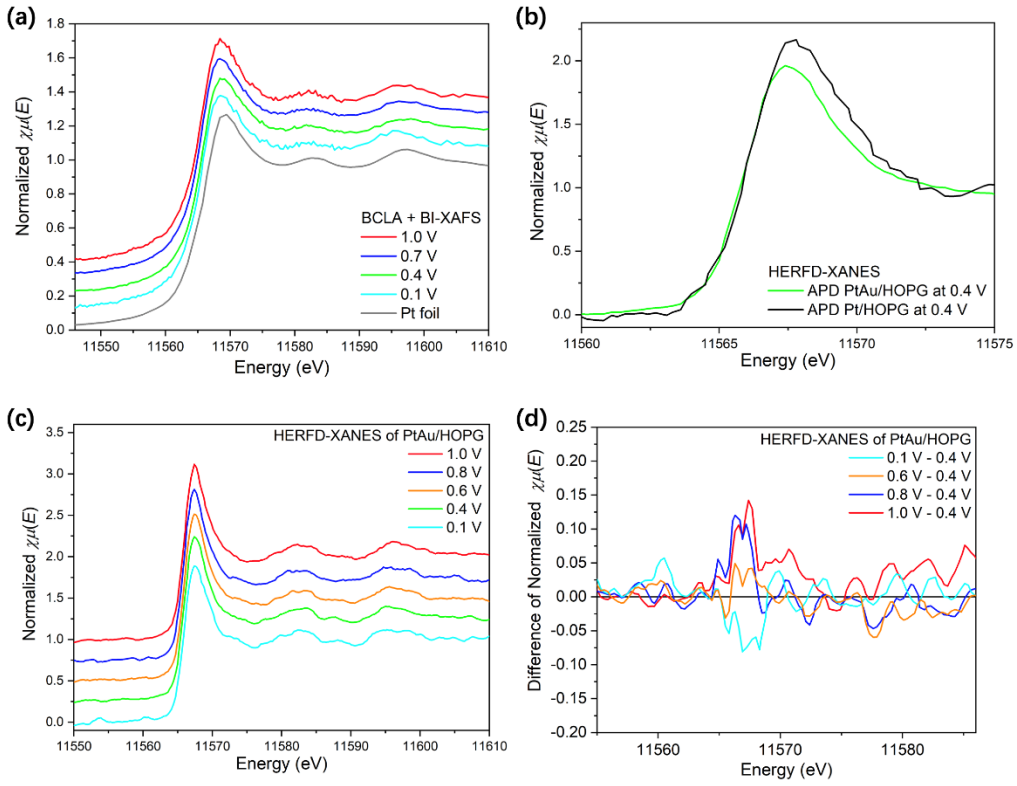

Figure 5 (a) BCLA + BI-XAFS Pt L_3 spectra of PtAu/HOPG at 0.1, 0.4, 0.7, and 1.0 V_{RHE}. (b) HERFD + BI-XANES of PtAu/HOPG and Pt/HOPG at 0.4 V_{RHE}. (c) Pt L_3 HERFD-XANES spectra of PtAu/HOPG measured at 0.1 , 0.4, 0.6, 0.8, and 1.0 V_{RHE}. (d) Pt L_3 HERFD difference spectra of PtAu/HOPG derived by subtracting the "clean-state" spectra at 0.4 V_{RHE}

from spectra recorded at other electrode potentials. All potentials are referenced to RHE.

PtAu Nanoparticle Structure at 0.4 V_{RHE}

Before starting the structure of PtAu nanoparticle structure, we should discuss the evidence for the formation of PtAu nanoparticle not formation of the Pt and Au segregated nanoparticle.

(1) The previous research on the synthesis of Au-Pt or Au-PtCo nanoparticles by the same arc plasma on the amorphous carbon film and STEM-EDX experiment showed the alloy formation of PtAu particles.[63]

(2) The cyclic voltammetry (CV) shows the less presence of Au on the surface of particles. If Au particles were present not in the alloy covered with Pt shell but in the pure Au, the particle size was estimated to be much more than 15 nm from the electrochemical surface area (ECSA) and XPS. But we could not find such large nanoparticle in the AFM.

(3) We found the electronic change in the PtAu nanoparticles compared to Pt nanoparticles as shown in Figure 5b.

(4) The abnormal contraction in Au-Au is another evidence for the PtAu alloying.

Consequently, we analyze the EXAFS data under the hypothesis that PtAu homogenous nanoparticle is formed on the HOPG surface. The Pt–*M* and Au–*M* bond lengths are approximately the same within the experimental error, similar to the Pt–Pt bond length in the Pt foil, and shorter than the Au–Au bond length in the Au foil.

We assume that:

(A) the bond lengths of Pt–*M* ($r_{\mathrm{Pt-}M}$) and Au–*M* ($r_{\mathrm{Au-}M}$) are both 2.76 Å;

(B) the $r_{\mathrm{Pt-}M}$ is obtained as the weighted average of the bond lengths of Pt–Pt ($r_{\mathrm{Pt-Pt}}$) and Pt–Au (r_{Pt-Au});

(C) similarly, $r_{\mathrm{Au-}M}$ is obtained as the weighted average of the bond lengths of Au–Pt ($r_{\mathrm{Au-Pt}}$) and Au–Au ($r_{\mathrm{Au-Au}}$).

Assumptions (B) and (C) can be expressed as

$$r_{\mathrm{Pt-}M} = x_{\mathrm{Pt-Pt}} \cdot r_{\mathrm{Pt-Pt}} + (1 - x_{\mathrm{Pt-Pt}}) \cdot r_{\mathrm{Pt-Au}} \quad (1)$$

$$r_{\mathrm{Au-}M} = (1 - x_{\mathrm{Au-Au}}) \cdot r_{\mathrm{Au-Pt}} + x_{\mathrm{Au-Au}} \cdot r_{\mathrm{Au-Au}} \quad (2)$$

$$x_{\mathrm{Pt-Pt}} = \frac{CN_{\mathrm{Pt-Pt}}}{CN_{\mathrm{Pt-}M}}, x_{\mathrm{Au-Au}} = \frac{CN_{\mathrm{Au-Au}}}{CN_{\mathrm{Au-}M}}. \quad (3)$$

The CNs of Au–Pt and Pt–Au should satisfy the following:

$$C_{\mathrm{Au}} \cdot (1 - x_{\mathrm{Au-Au}}) \cdot CN_{\mathrm{Au-}M} = C_{Pt} \cdot (1 - x_{\mathrm{Pt-Pt}}) \cdot CN_{\mathrm{Pt-}M}\,, \quad (4)$$

where C_{Au} and C_{Pt} are the compositions of Au and Pt, respectively.

$$C_{\mathrm{Au}} + C_{\mathrm{Pt}} = 1$$

Because $C_{\mathrm{Au}} : C_{\mathrm{Pt}} = 1 : 2.3$, $C_{\mathrm{Au}} \approx 0.3$. On the basis of the metallic radius, the following order must be true:

$$r_{\mathrm{Pt-Pt}} \leq r_{\mathrm{Pt-Au}} \leq r_{\mathrm{Au-Au}} \quad (5)$$

To satisfy equations (1)–(5) under assumption (A) ($r_{\mathrm{Pt}-M} \approx r_{\mathrm{Au}-M}$), we can conclude that

$$r_{\mathrm{Pt-Pt}} \approx r_{\mathrm{Pt-Au}} \approx r_{\mathrm{Au-Au}} \approx 2.76 \text{ Å}.$$

The Au–Au distance of 2.76 Å is abnormally short compared with that in Au foil. The CN of Pt is 8.6 ± 1.6, whereas that of Au is 11.0 ± 1.7. Because the CN of Pt ($CN_{\mathrm{Pt}-M}$) is much smaller than that of Au, the PtAu nanoparticles on HOPG should have a Pt-rich outer shell. Given the total CN of 9.3 [= (8.6 × 2.3 + 11.0 × 1)/(2.3 + 1)] and assuming a cuboctahedral PtAu nanoparticle structure, we propose that the PtAu nanoparticles are composed of 309 atoms (a five-shell structure with an average CN of 9.6). If the bond length within the 309-atom PtAu cuboctahedron is assumed to be a 2.76 Å, then the particle size between two facing (111) surfaces is ~20 Å, in agreement with that obtained from the AFM particle-height histogram. Because the Pt:Au ratio is 2.3:1, a $Pt_{215}Au_{94}$ cluster with a PtAu (core)–Pt-rich-shell structure (Figure 6a) can be assumed, in which the CNs of 8.8 and 11.6 for Pt and Au correspond well with the observed CNs within the error. In this model, the shell is predominantly Pt ($Pt_{155}Au_7$) and the core is composed of a smaller cuboctahedral M_{147} with a composition of $Pt_{60}Au_{87}$.

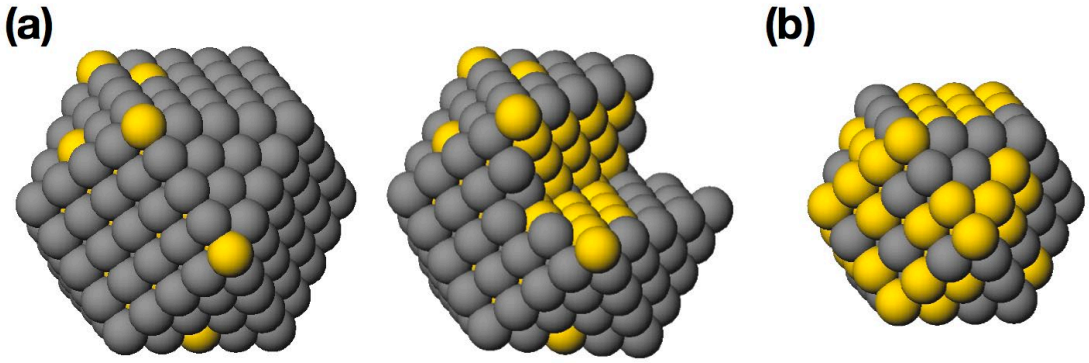

Figure 6 (a) $Pt_{215}Au_{94}$ model nanoparticles with a Pt CN of 8.8 and a Au CN of 11.6. (b) The inner shell of the $Pt_{215}Au_{94}$, which is $Pt_{60}Au_{87}$. Yellow and grey balls correspond to Au and Pt, respectively.

We found the following features in the structure of the PtAu subjected to an applied potential of 0.9 V_{RHE}:

I. The Au–*M* bond length is elongated to 2.80 Å, which is the average of the Au–Pt and Au–Au bond lengths in the nanoparticle.
II. Au is more abundant on the surface, as indicated by its lower CN.

III. The structure change observed at an applied potential of 0.9 V_{RHE} is attributed to the dissolution of Pt, and not to a change in the electronic state or the adsorbate.

If we assume that the Pt-rich shell is selectively removed and that ~48% of the Pt and ~91% of the Au remain in a nanoparticle, we can propose a model structure of a $Pt_{105}Au_{87}$ nanoparticle from the $Pt_{214}Au_{95}$ shown in Figure 6a, where the core region of the $Pt_{60}Au_{87}$ is maintained (Figure 6b) and is randomly covered with 45 Pt atoms. On the basis of the model shown in Figure 6, we can discuss the bonding features in the nanoparticle.

Explanation of the abnormal contraction of the Au–Au distance in PtAu/HOPG

The Au–*M* distance of 2.76 Å is much shorter than that for bulk Au (2.86 Å) and those previously reported (2.82–2.84 Å) in PtAu nanoparticles for both the alloy case[64,65] and the core–shell case.[21] The contraction of the metal bond distance in the nanoparticle is explained on the basis of the droplet model.[66] The contraction of the Au–*M* bond length, $\Delta r_{\mathrm{Au}-M}$, is expressed as

$$\Delta r_{\mathrm{Au}-M} = \frac{Afr_{\mathrm{Au}-M}K}{R} \qquad (6)$$

where A, $r_{\mathrm{Au}-M}$, f, K, and R are constant, the bulk bond length between Au and *M*, surface tension, the bulk compression rate, and the particle size, respectively. The value of *K* is similar for Pt and Au, whereas the value of f is different. The surface tension can be estimated from the cohesive energy density[67,68] and the surface tension is proportional to the square of the cohesive energy density. Because the cohesive energy for Au (cohesive energy = 3.81 eV $atom^{-1}$) is much smaller than that for Pt (5.84 eV $atom^{-1}$),[69] the surface tension should be 2.3 times greater in the Pt shell than in the Au shell. According to Miller et al.,[6] the expected contraction in a Au cluster of this size is 0.02 Å. Kaito et al.[21] found that for a Au(core)–Pt(shell) structure of similar size, the Au–Au bond length was contracted by 0.06 Å, which can be explained by a 2.3 times greater surface tension of the Pt shell compared with that of the Au shell. In the present case of PtAu (core)–Pt(shell), the contraction in the Au–Au bond length was 0.1 Å; that is, the Au–Au bond length was strongly contracted. This contraction can be explained by the shorter average bond length for $Au_{87}Pt_{60}$ (core), in which the average bond length was 2.82 Å = (60× 2.76 Å +87×2.86 Å). The 0.07 Å contraction from 2.82 Å gave a bond length of 2.75 Å, which is similar to the length we observed.

Such a short bond length in Au–*M* (2.77 Å) has been reported in PtAuCu supported on TPM-DPA-G4 (fourth-generation dendritic polyphenylazomethine tetraphenylmethane core) dendrimer.[70] The authors did not mention the origin of the short length or provide a detailed structure of the nanoparticle; however, we speculate that Cu remained in the

outermost shell because Cu exhibited the lowest CN among the three metals. The Cu outermost shell should compress the PtAu core more strongly, thereby leading to abnormal contraction. Kaito et al.[23] studied the Pt–Pt bond lengths in other bimetallic alloys such as PtCo, PtCu, and PtNi. Contrary to the Au core, the cores of these bimetallic systems have a smaller lattice, enabling easy contraction to give shorter Pt–Pt bond lengths.

When X-ray-facilitated electrochemical etching at potentials greater than 0.8 V_{RHE} removes a portion of the outermost Pt, the PtAu alloy core is exposed. $Pt_{60}Au_{87}$ + Pt_{45} is assumed to have formed on the basis of the core in Figure 6b, where numerous Au–Au bonds are present on the surface. The Au–*M* distance was elongated to 2.80 Å, whereas the Pt–*M* distance remained at 2.77 Å. Again, by considering assumptions (A)–(C) and equations (1)–(5), we can estimate an Au–Au distance of 2.83–2.81 Å, an Au–Pt distance of 2.79–2.77 Å, and a Pt–Pt distance of 2.75–2.73 Å. According to equation (6), the surface tension should be the average of the surface tensions of Pt and Au, and the contraction should be 0.03 to 0.04 Å (greater than that of 0.02 Å for a Au cluster), which corresponds to Au–Au and Pt–Pt distances of 2.83–2.82 Å and 2.75–2.74 Å, in agreement with the values obtained from the XAFS analysis.

The final question is why the Pt–Pt distance remains 2.76 Å in the $Pt_{60}Au_{87}$ (core)–$Pt_{155}Au_7$ (shell). This is because of the strong reduction of the Au–Au distance in the core region. This creates a large outward force that limits the reduction of the Pt–Pt distance in the shell. Moreover, the similar Pt–Pt, Pt–Au, and Au–Au distances in the $Pt_{60}Au_{87}$ (core)– $Pt_{155}Au_7$ (shell) nanoparticle relax the lattice distortion. Consequently, the original Pt–Pt bond length is retained. Our $Pt_{60}Au_{87}$ (core)– $Pt_{155}Au_7$ (shell) nanoparticle has a unique structure because of the large surface tension from the Pt-rich shell and the relaxation of the lattice distortion with the same metal–metal distance.

Difference in the Bond Length in Pt Overlayer on the Surface of a Single Crystal and Nanoparticles

We now return to the original question that motivated our research. The Pt–Pt bond contraction on the surface of Pt-shell nanoparticles is not due to an electronic effect because we did not observe a substantial difference in the XANES spectra during the change of Pt-Pt distance, even when using the HERFD + BI-XANES technique. The Pt shell structure on the surface of nanoparticles depends on two factors: (1) surface tension and (2) relaxation of the lattice distortion between the shell and core. Surface tension directed inward is proportional to R^{-1}, where R is the particle size or radius of curvature. The surface tension overcomes the relaxation of the lattice distortion between the Pt–Pt

shell and the core, resulting in contraction of the Pt–Pt bond length. However, the Pt overlayer structure on a flat single crystal surface depends only on the lattice distortion and the Pt–Pt distance is elongated to relax the lattice distortion between the Pt overlayer and the Au(111). Thus, flat single-crystal systems should be used judiciously as a model for functional nanoparticles in an alloy system.

CONCLUSIONS

Novel BCLA + BI-XAFS and HERFD + BI-XAFS methods were applied for *in situ* studies of the structure of PtAu/HOPG prepared by the APD method. Because of the high energy resolution of the BCLA (or the Ge bent-crystal monochromator), the interference from the Au L_3 edge could be removed entirely, enabling the acquisition of high-quality Pt L_3 XAFS spectra over a wide *k* region for a monolayer of PtAu nanoparticles, whose areal density was as low as 2×10^{15} cm^{-2} Pt, on an atomically flat HOPG surface. We also successfully recorded Au L_3 XAFS spectra.

XAFS analysis showed that, under an applied potential of 0.4 V_{RHE}, a cuboctahedral $Pt_{215}Au_{94}$ with a Pt-rich shell ($Pt_{155}Au_7$) and a compressed $Pt_{60}Au_{87}$ core was formed on the PtAu/HOPG model surface. We found an abnormally short Au−Au bond length of 2.76 Å, which was the same as the Pt−Pt and Au−Pt bond lengths. The abnormal contraction of the Au−Au distance was due to the strong surface tension from the Pt shell and the relaxation of the lattice distortion. The Pt−Pt distance in the Au(core)−Pt(shell) nanoparticles was contracted as a result of the surface tension of the nanoparticles. The surface tension was not present on the flat Au surface, and the Pt−Pt was elongated to relax the lattice distortion between the Pt overlayer and the Au(111) surface.

AUTHOR INFORMATION

Bing Hu, writer of the paper, the experiment leader, BI-XAFS, AFM, and XPS measurements and analyses
Bapurao Bharate,[†] BI-XAFS experiments
Juan D. Jimenez and Jochen Lauterbach, HERFD-BI-XANES experiments
Naoto Todoroki and Toshimasa Wadayama, sample preparation
Kotaro Higashi, Tomoya Uruga, Yasuhiro Iwasawa, BI-XAFS, conducted experiments
Hiroko Ariga-Miwa,[¶] Satoru Takakusagi[†], XAFS analysis and electrochemistry experiments
Kiyotaka Asakura[†*], experiment supervision

Corresponding Author
*E-mail: askr@cat.hokudai.ac.jp.
Notes
The authors declare no competing financial interest.

Supporting inromation is available.

Contents.
Experimental details

ACKNOWLEDGEMENT

The work was supported by the fuel cell project of NEDO (New Energy Development Organization) and now is supported by Grant-in-Aids for Scientific Research A (20H00367), Japan Society for the Promotion of Science (JSPS). Dr. Bing Hu is indebted to the funding support from the IRCCS of Hokkaido University. We are also grateful for the technical support provided by the technical division of ICAT, Hokkaido University. The experiments at Spring-8 were carried out under NEDO fuel cell projects with proposal Nos. 2019B7905, 2019B7904, 2019A7905, and 2018B7903. Dr. J. D. Jimenez was supported by the US National Science Foundation Interdisciplinary Graduate Education and Research Traineeship Program (IGERT) under grant number DGE-1250052.

REFERENCES

(1) Blackman, J. A. Metallic Nanoparticles; Misra, P., Ed. *Handbook of Metal Physics*; Elsevier: Amsterdam, The Netherlands, **2009**; Vol. 5.

(2) Maksimuk, S.; Teng, X.; Yang, H. Roles of Twin Defects in the Formation of Platinum Multipod Nanocrystals. J. *Phys. Chem. C* **2007**, *111*, 14312-14319.

(3) Sau, T. K.; Rogach, A. L. *Complex-Shaped Metal Nanoparticles: Bottom-Up Syntheses and Applications*; Wiley-VCH Verlag: Weinheim, Germany, **2012**.

(4) Apai, G.; Hamilton, J. F.; Stohr, J.; Thompson, A. *Extended* X- Ray-Absorption Fine Structure of Small Cu and Ni Clusters: Binding- Energy and Bond-Length Changes with Cluster Size*. Phys. Rev. Lett.* **1979**, *43*, 165−169.

(5) Chun, W.; Takakusagi, S.; Uemura, Y.; Bando, K.; Asakura, K. *in X-ray and Neutron Techniques for Nanomaterials*

Characterization; Kumar, C. S. S. R., Ed.;, Springer, Heidelberg, Germany, **2016**, pp. 609–664.

(6) Miller, J. T.; Kropf, A. J.; Zha, Y.; Regalbuto, J. R.; Delannoy, L.; Louis, C.; Bus, E.; van Bokhoven, J. A. The effect of gold particle size on AuAu bond length and reactivity toward oxygen in supported catalysts. *J. Catal.* **2006**, 240, 222-234.

(7) Lei, Y.; Jelic, J.; Nitsche, L. C.; Meyer, R.; Miller, J. Effect of particle size and adsorbates on the L 3, L 2 and L 1 X-ray absorption near edge structure of supported Pt nanoparticles. *Top. Catal.* **2011**, *54*, 334-348.

(8) Ohba, T.; Kubo, H.; Ohshima, Y.; Makita, Y.; Nakamura, N.; Uehara, H.; Takakusagi, S.; Asakura, K. EXAFS studies of Pd nanoparticles: direct evidence for unusual Pd–Pd bond elongation. *Chem. Lett.* **2015**, 44, 803-805.

(9) Ohba, T.; Kubo, H.; Ohshima, Y.; Makita, Y.; Nakamura, N.; Uehara, H.; Takakusagi, S.; Asakura, K. An Origin for Lattice Expansion in PVP-Protected Small Pd Metal Nanoparticles. *Bull. Chem. Soc. Jpn.* **2017**, *90*, 720-727.

(10) Kang, J. H.; Menard, L. D.; Nuzzo, R. G.; Frenkel, A. I. Unusual Non-Bulk Properties in Nanoscale Materials: Thermal Metal-Metal Bond Contraction of γ-Alumina-Supported Pt Catalysts. *J. Am. Chem. Soc.* **2006**, *128*, 12068-12069.

(11) Johnston, R. L.; Wilcoxon, J. P. *Metal Nanoparticles and Nanoalloys*; Elsevier: Amsterdam, The Netherland, **2012**; Vol. 3.

(12) Kodama, K.; Nagai, T.; Kuwaki, A.; Jinnouchi, R.; Morimoto, Y. Challenges in applying highly active Pt-based nanostructured catalysts for oxygen reduction reactions to fuel cell vehicles. *Nat. Nanotechnol.* **2021**, *16*, 140-147.

(13) Gottesfeld S.; Wieckowski, A.; Norskov *J. Fuel Cell Science: Theory, Fundamentals, and Biocatalysis*; John Wiley&Sons, **2011**.

(14) Zhang, J.; Sasaki, K.; Sutter, E.; Adzic, R. R. Stabilization of Platinum Oxygen-Reduction Electrocatalysts Using Gold Clusters. *Science* **2007**, *315*, 220–222.

(15) Takahashi, S.; Chiba, H.; Kato, T.; Endo, S.; Hayashi, T.; Todoroki, N.; Wadayama, T. Oxygen reduction reaction activity and structural stability of Pt–Au nanoparticles prepared by arc-plasma deposition. *Phys. Chem. Chem. Phys.* **2015**, *17*, 18638-18644.

(16) Higuchi, E.; Okada, K.; Chiku, M.; Inoue, H. Electrocatalytic activity for oxygen reduction reaction of Au core/Pt shell nanoparticle-loaded carbon black catalyst with different core sizes. *Electrochim. Acta* **2015**, *179*, 100-107.

(17) Tan, C.; Sun, Y.; Zheng, J.; Wang, D.; Li, Z.; Zeng, H.; Guo, J.; Jing, L.; Jiang, L. A self-supporting bimetallic Au@Pt core-shell nanoparticle electrocatalyst for the synergistic enhancement of methanol oxidation. *Sci. Rep.* **2017**, *7*, 1-10.

(18) Ren, X.; Lv, Q.; Liu, L.; Liu, B.; Wang, Y.; Liu, A.; Wu, G. Current progress of Pt and Pt-based electrocatalysts used for fuel cells. *Sustain. Energ. Fuels* **2020**, *4*, 15-30.

(19) Naya, S. I.; Miki, S.; Yamauchi, J.; Teranishi, M.; Kobayashi, H.; Tada, H. Au (Core)–Pt (Shell) Nanocatalysts with the Shell Thickness Controlled at a Monolayer Level: Extremely High Activity for Hydrogen Peroxide Decomposition. *J. Phys. Chem. C* **2018**, *122*, 22953-22958.

(20) Zhang, Y.; Li, X.; Li, K.; Xue, B.; Zhang, C.; Du, C.; ... Chen, W. Novel Au catalysis strategy for the synthesis of Au@Pt core–shell nanoelectrocatalyst with self-controlled quasi-monolayer Pt skin. *ACS Appl. Mater. Interfaces* **2017**, *9*,

32688-32697.

(21) Kaito, T.; Mitsumoto, H.; Sugawara, S.; Shinohara, K.; Uehara, H.; Ariga, H.; Takakusagi, S.; Hatakeyama, Y.; Nishikawa, K.; Asakura, K. K-edge X-ray absorption fine structure analysis of Pt/Au core–shell electrocatalyst: evidence for short Pt–Pt distance. *J. Phys. Chem. C* **2014**, *118*, 8481-8490.

(22) Adzic, R. R.; Zhang, J.; Sasaki, K.; Vukmirovic, M. B.; Shao, M.; Wang, J. X.; Nilekar, U.; Mavrikakis, J. A.; Uribe, F. Platinum monolayer fuel cell electrocatalysts. Top. Catal. **2007**, *46*, 249-262.

(23) Kaito, T.; Tanaka, H.; Mitsumoto, H.; Sugawara, S.; Shinohara, K.; Ariga, H.; Uehara, H.; Takakusagi, S.; Asakura, K. In situ X-ray absorption fine structure analysis of PtCo, PtCu, and PtNi alloy electrocatalysts: the correlation of enhanced oxygen reduction reaction activity and structure. *J. Phys. Chem. C* **2016**, *120*, 11519-11527.

(24) Mukerjee, S.; Srinivasan, S.; Soriaga, M. P.; McBreen, J. Role of structural and electronic properties of Pt and Pt alloys on electrocatalysis of oxygen reduction: an in situ XANES and EXAFS investigation. *J. Electrochem. Soc.* **1995**, *142*, 1409.

(25) Kim, J.; Jung, C.; Rhee, C. K.; Lim, T. H. Electrocatalytic oxidation of formic acid and methanol on Pt deposits on Au (111). *Langmuir* **2007**, *23*, 10831-10836.

(26) Zhang, J.; Vukmirovic, M. B.; Xu, Y.; Mavrikakis, M.; Adzic, R. R. Controlling the catalytic activity of platinum‐monolayer electrocatalysts for oxygen reduction with different substrates. *Angew. Chem. Int. Ed.* **2005**, *117*, 2170-2173.

(27) Uosaki, K.; Ye, S.; Naohara, H.; Oda, Y.; Haba, T.; Kondo, T. Electrochemical epitaxial growth of a Pt(111) phase on an Au(111) electrode. *J. Phys. Chem. B* **1997**, *101*, 7566-7572.

(28) Iwasawa, Y.; Asakura, K.; Tada, M., Eds.; *XAFS Techniques for Catalysts, Nanomaterials, and Surfaces*; Springer: Berlin, **2017**.

(29) Nagamatsu, S. I.; Arai, T.; Yamamoto, M.; Ohkura, T.; Oyanagi, H.; Ishizaka, T.; Kawanami, H.; Uruga, T.; Tada, M.; Iwasawa, Y. Potential-dependent restructuring and hysteresis in the structural and electronic transformations of Pt/C, Au(core)-Pt(shell)/C, and Pd(core)-Pt(shell)/C cathode catalysts in polymer electrolyte fuel cells characterized by in situ X-ray absorption fine structure. *J. Phys. Chem. C* **2013**, *117*, 13094-13107.

(30) Pearson, W. B. A *Handbook of Lattice Spacings and Structures of Metals and Alloys;* Pergamon Press: London, **1967**; Vol. 2.

(31) Mihut, C.; Descorme, C.; Duprez, D.; Amiridis, M. D. Kinetic and spectroscopic characterization of cluster-derived supported Pt–Au catalysts. *J. Catal.* **2002**, *212*, 125-135.

(32) Balakrishnan, K.; Sachdev, A.; Schwank, J. Chemisorption and FTIR study of bimetallic Pt Au/SiO2 catalysts. *J. Catal.* **1990**, *121*, 441-455.

(33) Song, C.; Ge, Q.; Wang, L. DFT studies of Pt/Au bimetallic clusters and their interactions with the CO molecule. *J. Phys. Chem. B* **2005**, *109*, 22341-22350.

(34) Luo, J.; Maye, M. M.; Petkov, V.; Kariuki, N. N.; Wang, L.; Njoki, P.; Mott, D.; Lin, Y.; Zhong, C. J. Phase properties of carbon-supported gold−platinum nanoparticles with different bimetallic compositions. *Chem. Mater.* **2005**, *17*, 3086-3091.

(35) Petkov, V.; Wanjala, B. N.; Loukrakpam, R.; Luo, J.; Yang, L.; Zhong, C. J.; Shastri, S. Pt–Au alloying at the nanoscale. *Nano Lett.* **2012**, *12*, 4289-4299.

(36) Irissou, E.; Laplante, F.; Garbarino, S.; Chaker, M.; Guay, D. Structural and electrochemical characterization of

metastable PtAu bulk and surface alloys prepared by crossed-beam pulsed laser deposition. *J. Phys. Chem. C* **2010**, *114*, 2192-2199.

(37) Deng, L.; Hu, W.; Deng, H.; Xiao, S. Surface segregation and structural features of bimetallic Au−Pt nanoparticles. *J. Phys. Chem. C* **2010**, *114*, 11026-11032.

(38) Ramaker, D. E.; Koningsberger, D. C. The atomic AXAFS and Δμ XANES techniques as applied to heterogeneous catalysis and electrocatalysis. *Phys. Chem. Chem. Phys.* **2010**, *12*, 5514-5534.

(39) Allen, P. G.; Conradson, S. D.; Wilson, M. S.; Gottesfeld, S.; Raistrick, I. D.; Valerio, J.; Lovato, M. In situ structural characterization of a platinum electrocatalyst by dispersive X-ray absorption spectroscopy. *Electrochim. Acta* **1994**, *39*, 2415-2418.

(40) Tada, M.; Murata, S.; Asakoka, T.; Hiroshima, K.; Okumura, K.; Tanida, H.; Uruga, T.; Nakanishi, H.; Matsumoto, S.; Inada, Y.; Nomura, M.; Iwasawa, Y. In situ time‐resolved dynamic surface events on the Pt/C cathode in a fuel cell under operando conditions. *Angew. Chem. Int. Ed.* **2007**, *46*, 4310-4315.

(41) Nitani, H.; Nakagawa, T.; Daimon, H.; Kurobe, Y.; Ono, T.; Honda, Y.; Koizumi, A.; Seino, S.; Yamamoto, T. A. Methanol oxidation catalysis and substructure of PtRu bimetallic nanoparticles. *Appl. Catal. A: Gen.* **2007**, *326*, 194-201.

(42) Sasaki, K.; Wang, J. X.; Naohara, H.; Marinkovic, N.; More, K.; Inada, H.; Adzic, R. R. Recent advances in platinum monolayer electrocatalysts for oxygen reduction reaction: Scale-up synthesis, structure and activity of Pt shells on Pd cores. *Electrochim. Acta* **2010**, *55*, 2645-2652.

(43) Takao, S.; Sekizawa, O.; Samjeske, G.; Nagamatsu, S. I.; Kaneko, T.; Yamamoto, T.; Higashi, K.; Nagasawa, K., Uruga, T.; Iwasawa, Y. Same-view nano-XAFS/STEM-EDS imagings of Pt chemical species in Pt/C cathode catalyst layers of a polymer electrolyte fuel cell. *J. Phys. Chem. Lett.* **2015**, *6,* 2121-2126.

(44) Sekizawa, O.; Uruga, T.; Higashi, K.; Kaneko, T.; Yoshida, Y.; Sakata, T.; Iwasawa, Y. Simultaneous operando time-resolved XAFS–XRD measurements of a Pt/C cathode catalyst in polymer electrolyte fuel cell under transient potential operations. *ACS Sustain. Chem. Eng.* **2017**, 5, 3631-3636.

(45) Uehara, H.; Uemura, Y.; Ogawa, T.; Kono, K.; Ueno, R.; Niwa, Y.; Nitani, Y.; Abe, H.; Takakusagi, S.; Nomura, M.; Iwasawa, Y.; Asakura, K. In situ back-side illumination fluorescence XAFS (BI-FXAFS) studies on platinum nanoparticles deposited on a HOPG surface as a model fuel cell: a new approach to the Pt-HOPG electrode/electrolyte interface. *Phys. Chem. Chem. Phys.* **2014**, *16*, 13748-13754.

(46) Wakisaka, Y.; Hu, B.; Kido, D.; Al Rashid, M. H.; Chen, W.; Dong, K.; Wada, T.; Bharate, B.; Yuan, Q.; Mukai, S.; Takeichi, Y.; Takakusagi, S.; Asakura, K. Bent crystal Laue analyser combined with total reflection fluorescence X-ray absorption fine structure (BCLA+ TRF-XAFS) and its application to surface studies. *J. Synchrotron Radiat.* **2020**, *27*, 1618-1625.

(47) Asakura, K. in X-ray Absorption Fine Structure for Catalyst and Surfaces; Iwasawa, Y., Ed.; World Scientific: Singapore, **1996**; pp 33-58.

(48) Uruga, T.; Tada, M.; Sekizawa, O.; Takagi, Y.; Yokoyama, T.; Iwasawa, Y. SPring‐8 BL36XU: Synchrotron Radiation X‐Ray‐Based Multi‐Analytical Beamline for Polymer Electrolyte Fuel Cells under Operating Conditions. *Chem. Rec.* **2019**, *19*, 1444-1456.

(49) Park, S.; Yang, P.; Corredor, P.; Weaver, M. J. Transition metal-coated nanoparticle films: vibrational characterization with surface-enhanced Raman scattering. *J. Am. Chem. Soc.* **2002**, 124, 2428-2429.
(50) Rodriguez, P.; Garcia-Araez, N.; Koper, M. T. Self-promotion mechanism for CO electrooxidtion on gold. *Phys. Chem. Chem. Phys.* **2010**, *12*, 9373-9380.
(51) Fung, S. C. Application of XPS to the determination of the size of supported particles in a catalyst—Model development and its application to describe the sintering behavior of a silica-supported Pt film. *J. Catal.* **1979**, *58*, 454-469.

[52] Feiten, F. E.; Takahashi, S.; Sekizawa, O.; Wakisaka, Y.; Sakata, T.; Todoroki, N.; Uruga, T.; Wadayama, T.; Iwasawa, Y.; Asakura, K. Model building analysis–a novel method for statistical evaluation of Pt L 3-edge EXAFS data to unravel the structure of Pt-alloy nanoparticles for the oxygen reduction reaction on highly oriented pyrolytic graphite. *Phys. Chem. Chem. Phys.* **2020**, 22, 18815-18823.

(53) Plackett, R. L. Karl Pearson and the chi-squared test. *Int. Stat. Rev.* **1983**, 59-72.
(54) Chun, W.-J.; Asakura, K.; Iwasawa, Y., Polarization-dependent total-reflection fluorescence XAFS study of Mo oxides on a Rutile TiO_2(110) single crystal surface. *J.Phys.Chem.* **1998**, *102*, 9006-9014.

(55) de Groot, F. M. F.; Kotani, A. *Core Level Spectroscopy of Solids*; CRC Press: Boca Raton, FL, **2008**.
(56) Krause, M. O.; Oliver, J. H. Natural widths of atomic K and L levels, Kα X‐ray lines and several KLL Auger lines. *J. Phys. Chem. Ref. Data* **1979**, 8, 329-338.
(57) Clavilier, J.; Armand, D. Electrochemical induction of changes in the distribution of the hydrogen adsorption states on Pt (100) and Pt (111) surfaces in contact with sulphuric acid solution. *J. Electroanal. Chem. Interf. Electrochem.* **1986**, *199*, 187-200.

(58) Bard, A. J.; Faulkner, L. R. *Electrochemical Methods: Fundamentals and Applications;* John Wiley&Sons, **2000**.

(59) Asakura, K.; Kubota, T.; Ichikuni, N.; Iwasawa, Y. in *Stud. Surf.Sci.Catal.* Hightower, J. W.; Delgass, W. N.; Iglesia, E.; Bell, A. T., Eds. Elsevier Science :Amsterdam the Netherland, **1996**; Vol101, pp 911-919.
(60)Kubota, T.; Asakura, K.; Ichikuni, N.; Iwasawa, Y., A New Method for Quantitative Characterization of Adsorbed Hydrogen on Pt Particles by Means of Pt L-Edge Xanes. *Chem. Phys. Lett.* **1996**, *256*, 445-448.
(61) Reifsnyder, S. N.; Otten, M. M.; Sayers, D. E.; Lamb, H. H. Hydrogen chemisorption on Silica-supported Pt clusters: In situ X-ray absorption spectroscopy. *J. Phys. Chem. B* **1997**, *101*, 4972-4977.
(62) Bus, E.; van Bokhoven, J. A. Hydrogen chemisorption on supported platinum, gold, and platinum–gold-alloy catalysts. *Phys. Chem. Chem. Phys.* **2007**, *9*, 2894-2902.

(63) Takahashi, S., et al., Effective Surface Termination with Au on Ptco@Pt Core-Shell Nanoparticle: Microstructural Investigations and Oxygen Reduction Reaction Properties. *J Electroanal Chem* **2019**, *842*, 1-7.

(64) Lapp, A. S.; Duan, Z.; Marcella, N.; Luo, L.; Genc, A.; Ringnalda, J.; Frenkel, A. I.; Henkelman, G.; Crooks, R. M.

Experimental and theoretical structural investigation of AuPt nanoparticles synthesized using a direct electrochemical method. *J. Am. Chem. Soc.* **2018**, *140*, 6249-6259.

(65) Xu, Z.; Kibria, M. G.; AlOtaibi, B.; Duchesne, P. N.; Besteiro, L. V.; Gao, Y.; Zhang, Q.; Mi, Z.; Zhang, P.; Govorov, A. O.; Mai, L.; Chaker, M.; Ma, D. Towards enhancing photocatalytic hydrogen generation: Which is more important, alloy synergistic effect or plasmonic effect? *Appl. Catal. B: Environ.* **2018**, *221*, 77-85.

(66) Mays, C. W.; Vermaak, J. S.; Kuhlmann-Wilsdorf, D. On surface stress and surface tension: II. Determination of the surface stress of gold. *Surf. Sci.* **1968**, *12*, 134-140.

(67) Schonhorn, J. Theoretical Relationship between Surface Tension and Cohesive Energy Density. *J. Chem. Phys.* **1965**, 43, 2041-2043.

(68) Becher, P. The calculation of cohesive energy density from the surface tension of liquids. *J. Colloid Interface Sci.* **1972**, 38, 291-293.

(69) Kittel, C. Introduction to Solid State Physics, 8th Edition; Wiley: New York, **2004**.

(70) Takahashi, M.; Koizumi, H.; Chun, W. J.; Kori, M.; Imaoka, T.; Yamamoto, K. Finely controlled multimetallic nanocluster catalysts for solvent-free aerobic oxidation of hydrocarbons. *Sci. Adv.* **2017**, 3, e1700101

(56)

(57)

(58)

(59)

(60)

(61)

(62)

(63)

(64)

(65) Mays, C. W.; Vermaak, J. S.; Kuhlmann-Wilsdorf, D. On surface stress and surface tension: II. Determination of the surface stress of gold. *Surf. Sci.* **1968**, 12, 134-140.

(66)

(67)

(68)

(69)

Hamilton, W. C. Significance tests on the crystallographic R factor. *Acta Crystallogr.* **1965**, 18, 502-510.

(1)

(2) Maksimuk, S.; Teng, X.; Yang, H. Roles of Twin Defects in the Formation of Platinum Multipod Nanocrystals. J. Phys. Chem. C **2007**, 111, 14312-14319.

(3)

(5)

(13)